Phonon thermal conductance across GaN-AlN interfaces from first principles

Carlos A. Polanco and Lucas Lindsay

Phys. Rev. B **99**, 075202 — Published 8 February 2019

DOI: 10.1103/PhysRevB.99.075202

Phonon thermal conductance across GaN-AlN interfaces from first-principles

Carlos A. Polanco and Lucas Lindsay
Materials Science and Technology Division, Oak Ridge National Laboratory, Oak Ridge, Tennessee 37831, USA

Phonon thermal conductance across GaN-AlN interfaces from first-principles

Carlos A. Polanco and Lucas Lindsay
Materials Science and Technology Division, Oak Ridge National Laboratory, Oak Ridge, Tennessee 37831, USA

Abstract

The vibrational thermal conductances (*G*) across GaN-AlN interfaces are computed using a non-equilibrium Green's functions formalism in the harmonic limit with bulk and interfacial interatomic force constants (IFCs) fully from density functional theory. Several numerical methods and supercell configurations are employed to examine the sensitivity of G to variances of IFCs. In particular, the effects of supercell size, the enforcement of symmetry constraints and truncation of IFCs near the interface, and atomic relaxation on phonon transmission and conductance are explored. Our fully first-principles calculations are compared with common approximations and measured *G* values inferred from thermal conductivity measurements for GaN-AlN superlattices. Our calculated value, $G \sim 300$ MWm^{-2}K^{-1}, is nearly half that from measurements. This discrepancy is critically analyzed in terms of the physical assumptions of the calculations and the derivation of the experimental values. This work provides guidelines to determine 'physically correct' sets of interfacial IFCs from first-principles for thermal conductance calculations using minimal computational resources. It also contributes towards developing predictive calculations and a more complete picture of thermal conduction across interfaces, a first step toward first-principles multiscale thermal transport.

I. INTRODUCTION

During the last decade, predictive calculations of phonon thermal conductivity of single crystals have flourished [1–8], opening the possibility to design materials with targeted and extreme thermal functionalities computationally [9–14]. The theoretical and numerical framework behind these calculations has also allowed for refinement of our fundamental understanding of transport processes, like providing new rules of thumb for three-phonon scattering [9,15,16]. Extending this existing framework to systems with broken symmetry, e.g., including defects and interfaces presents significant challenges. Yet, such capabilities will expand the existing computational design effort of thermal properties to nanostructured materials, multi-material systems and devices. Moreover, such a framework has the potential to enrich our fundamental understanding of vibrational properties and phonon transport near and across interfaces, building a more comprehensive picture of these in coupled material systems.

Creating a predictive framework for interface thermal conductance has several challenges, including benchmarking it. From a modeling point of view, thermal measurements on well-characterized simple structures are desired. However, atomic structures near an interface are complicated. Atoms are not at ideal crystal positions, even diffusing into neighboring materials forming defects to release lattice stress [17]. Interfaces can vary from sample to sample and structural characterization is limited to a few non-trivial techniques, including 2D transmission electron microscopy and x-ray diffraction. Thermal conductance measurements invoke assumptions that limit sensitivity [18] and measured values of conductance on clean interfaces between commensurate crystals are scarce [19–24]. Interface conductance can also be inferred from the thermal conductivity of superlattices using resistive additive models, however, such models often ignore important lattice wave effects near and between interfaces [25,26].

Modeling heat flow across interfaces has its own challenges. Calculating the various interatomic force constants (IFCs) required to describe vibrations and transport for interface atomic configurations from density functional theory (DFT) requires a large computational effort. Furthermore, state-of-the-art first-principles methodologies to describe interfacial transport are missing key physical features: the Boltzmann equation neglects the wave nature of phonons, molecular dynamics calculations neglect their quantum nature and non-equilibrium Green's function (NEGF) methods neglect anharmonic interactions. Note NEGF methods can include anharmonic interactions [27–30], but to the best of our knowledge it has not been done from first-principles. The first '*ab-initio*' interface conductance simulations only included mass variance effects, using IFCs from a single bulk material and fully neglecting IFC variations at the interfaces [31–33]. Others employed *ad hoc* assumptions to define the IFCs near the interface [34]. More recent calculations on Gold–Alkane [35], Cu/Graphene/Cu [36] and silicide-silicon [37] interfaces have computed interfacial IFCs more rigorously from 'first-principles'. These studies have shown that using simple averages of interfacial IFCs can overestimate the conductance by up to 70% [37], thus demonstrating their importance for rigorous interface conductance predictions.

Numerical calculation of interfacial IFCs and conductance from DFT and Green's functions requires careful consideration of several variables, including supercell and interface sizes, IFC truncation, connecting interface regions with bulk contact materials, etc. Yet, systematic exploration of these numerical nuances, particularly toward achieving the correct physical picture of interface conductance with minimal computational cost, is lacking. In this paper, we present a thorough study of interface conductance as determined by first-principles IFCs derived from different numerical methods and supercell configurations. The effects of supercell size, interaction truncation distance from the interface, symmetry and invariance enforcement and atomic relaxation on phonon mode transmission and overall conductance are explored. Physically meaningful IFCs are determined by the finite displacement (FD) method, which eases the computational cost over other perturbative approaches as only required IFCs near the interface are calculated.

Our study focuses on the interface of GaN and AlN (wide band gap, polar semiconductors with wurtzite structure) largely due to: (1) their technological relevance as basic components of high-electron mobility transistors [38,39] and optical devices [40,41]; (2) availability of thermal conductivity measurements on epitaxially grown GaN-AlN superlattices [25] with high interfacial quality [42]; and (3) thermal transport is dominated by phonons. Long-range, non-analytic polar interactions are important for describing the optical vibrations of these materials. These interactions are not well captured by real space methods, such as FD methods and non-equilibrium Green's functions. Uncertainty and limitations of these approaches are evaluated in this work.

Complementing this numerical exploration of the GaN-AlN interface, calculations are critically compared with values inferred from experiments demonstrating significant discrepancies. Using these microscopic vibrational conductance calculations, we assess assumptions, both here and in deriving experimental values, compare with common approximations and develop a more complete physical understanding of thermal transport across interfaces. This work will enable calculations of other important interfacial systems toward a more complete picture of thermal properties of devices.

II. METHODS

Describing and simulating an interface of materials - a non-periodic system - from periodic structures constructed by typical DFT methods is nontrivial, requiring definition of the interface region, careful consideration of the supercell building blocks and linking of the various material regions. For example, a perfectly abrupt interface of two materials has a finite spatial region for which the relaxed atomic positions and IFCs vary from the bulk constituent materials. A key task of this research effort is to characterize this region in a numerically efficient manner, balancing quantitative accuracy with computational cost.

For our Green's function description, GaN-AlN interfaces are divided into three regions: left contact (bulk GaN), right contact (bulk strained AlN (sAlN)), and device (comprised of blocks of

both GaN and sAlN primitive unit cells (uc)) as shown in Figure 1a. The IFCs of the contact regions are derived from supercells built from their relaxed primitive uc (two group III atoms and two N atoms with wurtzite structure as shown in Figure 1b), just as with typical bulk crystal calculations. AlN is strained in-plane to match the lattice of GaN to most closely correlate with available experimental data (see Section III).

For the device region, the goal is to describe a single interface from periodic structures (see Figure 1a and b). This requires building an interface cell with a sufficient number of uc perpendicular to the material junction (defined here along the z axis), truncating the interactions of these so that periodically replicated interfaces of the 'superlattice' do not artificially interfere, and connecting the truncated piece to the bulk constituent materials of the interface. To determine interfacial IFCs, an interface cell of length L_{cell} (measured in uc) is built from $L_{cell}/2$ primitive unit cells of GaN on the left of the interface and $L_{cell}/2$ primitive unit cells of sAlN on the right. This cell is allowed to relax along the z direction (see Appendix A) and then it is stacked in the x and y directions to create a $W \times W \times L_{cell}$ supercell (example shown in Figure 1c for $W = 4$ uc and $L_{cell} = 8$ uc).

To build the IFCs of the device region for the Green's function calculations, the IFCs from the interface cell are restricted to length L_{cut} of the interface. This reduced region is sandwiched between bulk GaN and sAlN as shown in Figure 1a. The restricted interface length L_{cut} should be less than half the interface cell length L_{cell}, but long enough so that atoms near its far edges have IFCs similar to those of the bulk materials. This avoids including the spurious interactions from periodically replicated interfaces, while allowing more seamless connection to the bulk contacts. IFCs connecting two atoms from different regions are set to the corresponding IFCs from bulk GaN and sAlN. At this point, the IFCs from all regions, except those coming from the reduced region, satisfy derivative permutation, space group, translational and rotational invariances because those symmetries were enforced on the bulk crystals. Thus, we enforce these on the remaining atoms by slightly modifying IFCs for interacting atoms within the reduced region. Details of the calculations are given in Appendix A.

IFCs are calculated by numerical differentiation of atomic forces in supercells, the so-called finite displacement method. Atomic forces are extracted from self-consistent energy computations using the pw.x module of Quantum Espresso [43]. Some caveats for these calculations are discussed in Sec. IV.

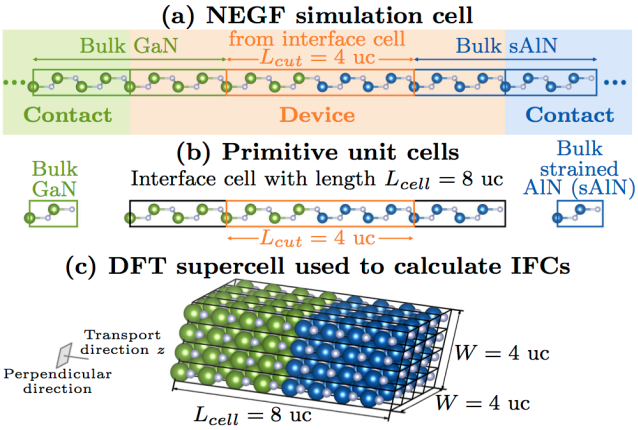

Figure 1: (a) Sample simulation cell consisting of device (red shaded region containing the interface) and contacts (bulk materials). This cell is repeated transverse to the interface to form the NEGF simulation system. (b) Schematic of the primitive unit cells of the GaN-sAlN interface region with length $L_{cell} = 8$ uc, and bulk GaN and sAlN contacts. The device is built by sandwiching a region of restricted length L_{cut} within the interface cell, between bulk GaN and sAlN. (c) $W \times W \times L_{cell}$ supercell, with $W = 4$ uc, built by repeating primitive interface unit cells (uc) with length $L_{cell} = 8$ uc, half GaN and half sAlN.

Thermal conductance G is defined as the ratio between induced heat flux and applied temperature gradient. In the harmonic limit, where phonons do not interact, the conductance of a device (region surrounding the interface shown in Figure 1a) connected to contacts (bulk sAlN and GaN as shown in Figure 1a) at thermal equilibrium can be expressed according to the Landauer formalism as [44]

$$G = \frac{1}{A}\int_0^\infty \frac{d\omega}{2\pi} C(\omega) MT(\omega) \tag{1}$$

with A the cross-sectional area, ω the phonon frequency, $C(\omega) = \hbar\omega \frac{\partial N(\omega)}{\partial T}$ the mode heat capacity, $\hbar$ the reduced Planck's constant, $N(\omega)$ the Bose-Einstein distribution, T the temperature and; $MT(\omega)$ the sum of transmissions between all available phonons in the contacts, which is computed using non-equilibrium Green's functions (NEGF) [45]. The NEGF outcome is labeled $MT(\omega)$ to highlight the wave and quantized nature of phonon transport. $M(\omega)$ represents the number of modes or available transport channels at frequency ω, while $T(\omega)$ represents an average phonon transmission over those channels. $M(\omega)$ is closely related to the quantum of thermal conductance [44] and defines an upper bound of conductance (when phonons flow ballistically $T(\omega) = 1$), which arises from intrinsic scattering processes necessary to bring phonons to thermal equilibrium at the contacts [45]. $M(\omega)$ is an integer number and can also be determined by counting the number of 1D phonon bands crossing ω along the transport direction. Thus, $M(\omega)$ is sometimes referred to as the number of available transport channels [45]. On the other hand, $T(\omega)$ captures an average of wave scattering properties of phonons. For instance in a simple 1D chain with one phonon band ($M(\omega)$=1), $MT(\omega)$ from NEGF matches the wave transmission found by solving the scattering problem of an impinging vibrational wave on a device [46,47].

When the system (device plus contacts) is periodic in the plane perpendicular to transport (Figure 1c), as is the case for an abrupt interface, the calculation of $MT(\omega)$ is simplified by Fourier transforming the atomic coordinates perpendicular to transport into reciprocal space. This step turns the 3D system into decoupled 1D chains whose contributions can be calculated independently so that $MT(\omega)$ is given by [28,45,48,49]

$$MT(\omega) = \sum_{\vec{q}_\perp} MT_{\vec{q}_\perp}(\omega) = \sum_{\vec{q}_\perp} \mathrm{Trace}\left\{\Gamma^L_{\vec{q}_\perp}(\omega) G^r_{\vec{q}_\perp}(\omega) \Gamma^R_{\vec{q}_\perp}(\omega) \left(G^r_{\vec{q}_\perp}(\omega)\right)^\dagger\right\} \qquad (2)$$

with $\vec{q}_\perp$ a 2D wavevector perpendicular to transport running over a 2D Brillouin zone that labels each decoupled 1D chain. $\Gamma^\alpha_{\vec{q}_\perp}(\omega)$ with $\alpha = L, R$ are the broadening matrices from the left and right contacts and $G^r_{\vec{q}_\perp}(\omega)$ is the retarded Green's function of the $\vec{q}_\perp$ 1D chain. The Green's functions describe the dynamics of atomic vibrations in the device portion of each chain, while the broadening matrices describe the lifetimes of those phonons escaping to the contacts [45]. Note that the Green's functions are solutions of the many-body atomic equation of motion and thus captures the wave and quantum nature of atomic vibrations in the device. A description of the steps required to calculate $\Gamma^\alpha_{\vec{q}_\perp}(\omega)$ and $G^r_{\vec{q}_\perp}(\omega)$ from a given set of IFCs is given in Appendix A. In the following sections, $MT(\omega)$ is plotted as an average over decoupled 1D chains $\langle MT(\omega)\rangle_{\vec{q}_\perp} = MT(\omega)/N_{\vec{q}_\perp}$ with $N_{\vec{q}_\perp}$ the number of 1D chains or grid points in the 2D Brillouin zone.

III. COMPARING THEORY WITH MEASUREMENTS

Our conductance calculations versus temperature for two perfectly abrupt GaN-sAlN interfaces are given in Figure 2b, one with Al-N bonds at the interface (type 1, solid black curve) and the other with Ga-N bonds (type 2, solid red curve), see schematic in Figure 2a. Interfacial IFCs were determined from supercell structures with $W = 4$ uc and $L_{cell} = 8$ uc. These were truncated near the material junction to include an interface length $L_{cut} = 4$ uc in our simulation system as depicted in Figure 1. The overall G for both interface types are similar, despite their spectral contributions, which are proportional to $MT(\omega)$, being different (Figure 2d). For instance, phonons around 7 THz are 30% more likely to cross a type 2 interface than a type 1 interface. Note that type 1 interfaces are energetically favorable [41]. When GaN is strained in-plane (sGaN) to match the lattice of AlN, *G* at room temperature for a type 1 sGaN-AlN interface is only 5% larger than that of its counterpart GaN-sAlN interface. Most of the difference arises from optical vibrations above the phonon bandgap that shift upward in frequency as GaN contracts in-plane.

For comparison, Figure 2b also shows G as determined by the diffuse mismatch model (DMM) obtained by replacing $MT(\omega)$ in Eq. 1 with [35]

$$MT_{DMM}(\omega) = \frac{M_{GaN}(\omega)M_{sAlN}(\omega)}{M_{GaN}(\omega) + M_{sAlN}(\omega)} \quad (3)$$

where $M_{GaN}(\omega)$ and $M_{sAlN}(\omega)$ are calculated from Eq. 2 assuming the device and contacts are either GaN or sAlN which yields $T(\omega) = 1$. $M(\omega)$ then counts the number of propagating modes or transport channels available in either bulk material. This DMM conductance is built from first-principles dispersions of GaN and sAlN. $MT_{DMM}(\omega)$ is a parallel combination of available transport channels in the contacts so it is large whenever both $M_{GaN}(\omega)$ and $M_{sAlN}(\omega)$ are large. Figure 2d shows that $MT_{DMM}(\omega)$ is much larger than $MT(\omega)$ for type 1 and type 2 interfaces, which happens because $MT(\omega)$ is bounded by the available transport channels in the contacts that conserve momentum parallel to the interface [32]. The extra momentum conservation constraint diminishes $MT(\omega)$ and conductance with respect to that from the DMM (Figure 2b).

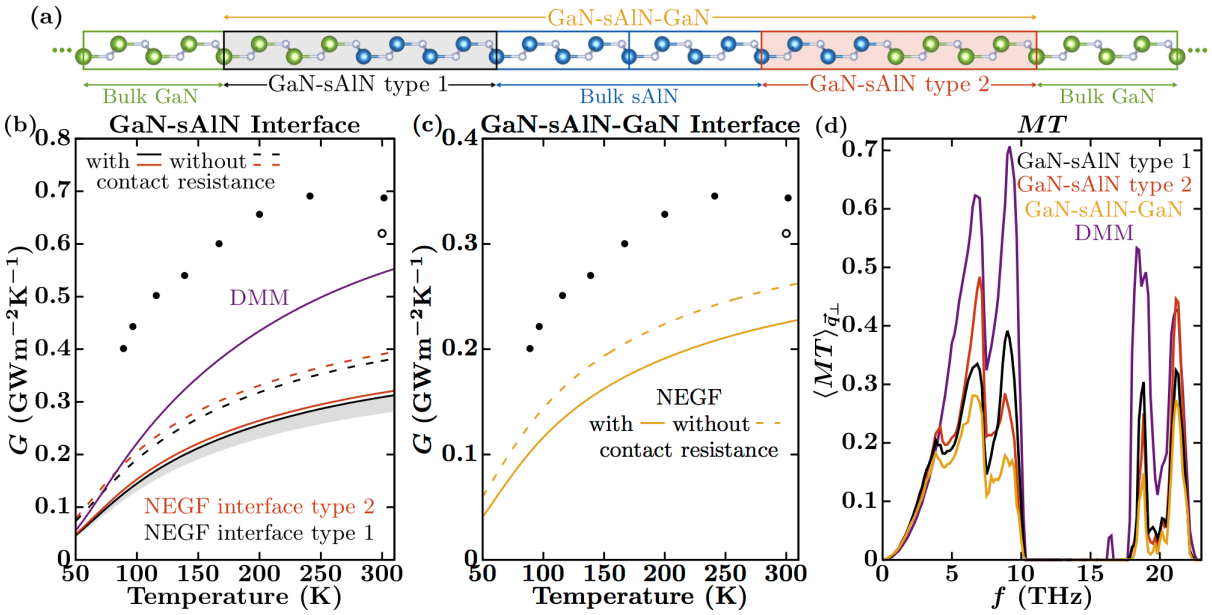

Figure 2: (a) Schematic of the simulated single and double interfaces. (b) Comparison of first-principles G for a GaN-sAlN interface with the diffuse mismatch model (DMM) and with data inferred from GaN-sAlN superlattice experiments (symbols [25]). Solid curves give G directly from calculations, while dashed curves give G with contact resistances excluded (see text). The shaded region represents the numerical uncertainty in the calculation of the black curve. (c) First-principles G of a GaN-sAlN-GaN double interface compared with data determined from experiments. (d) Average $MT(\omega)$ per unit cell in the interfacial plane (see Section II) for the interfaces described in (a).

Figure 2b compares calculated interface conductance values with values inferred from thermal conductivity measurements of GaN-AlN superlattices κ_{SL} [25]. The superlattices were grown using molecular beam epitaxy to achieve high quality interfaces with estimated interdiffusion and interfacial roughness $\lesssim 1$ nm [38,42]. Each sample was grown on a 3.6 μm GaN buffer starting and ending with AlN and keeping the thickness of AlN layers at ~4 nm [25] so that the bulk of the

AlN material strains to lattice-match with GaN (~53 nm thick) avoiding dislocations and cracks [25]. κ_{SL} was measured using time-domain thermoreflectance [25], while the conductance of individual interfaces G was inferred assuming the thermal resistance of a superlattice period is the sum of the resistances of the interfaces and layers [25]

$$\frac{z_{GaN}+z_{AlN}}{\kappa_{SL}}=\frac{z_{GaN}}{\kappa_{GaN}}+\frac{z_{AlN}}{\kappa_{AlN}}+\frac{2}{G} \quad (4)$$

with z_{GaN} (z_{AlN}) the thickness of GaN (AlN) layers and κ_{GaN} and κ_{AlN} their corresponding thermal conductivities, which were taken to be the largest measured values in the literature (Appendix B). Note that smaller κ_{GaN} and κ_{AlN} yield larger values of G. Figure 2b shows the extracted G from Eq. 4 with $z_{GaN}=53$ nm (open dot comes from Figure 3a while filled dots from Figure 5 in [25]). The 10% difference of measured values at room temperature manifests from the uncertainty of the κ_{SL} measurements (ranging from 18.07 to 16.44 $Wm^{-1}K^{-1}$). Note that Eq. 4 assumes that all phonons crossing an interface reach thermal equilibrium near it. This approximation is not fully justified, particularly near the 4nm AlN layer, however it provides an initial reference point to develop further understanding of phonon transport across interfaces in superlattice structures [26,50].

The calculated G for both types of GaN-sAlN interfaces (black and red solid curves in Figure 2b) are ~45% of the measured value extracted from GaN-AlN superlattices with $z_{GaN}=53$ nm at room temperature (filled dots in Figure 2b). This difference is not expected to decrease when improving numerical convergence of the calculations (see Section IV), since increasing W, L_{cell} and L_{cut} decrease the conductance value by about 10% (shaded region in Figure 2b). The discrepancy with experiments is partly due to our assumptions: calculated *G* are obtained (1) in the harmonic limit (neglecting phonon-phonon interactions), (2) on perfectly abrupt interfaces (neglecting interatomic mixing), and (3) including additional contact resistances (not present in experimental values). Furthermore, the assumption in Eq. 4 that all of the individual interface resistances can be simply added is questionable given that some of the GaN-AlN superlattice interfaces are only 4nm apart. These factors are critically analyzed in the rest of this section.

Part of the difference between calculated and measured *G* arises from artificial contact resistance in NEGF calculations. Eq. 1 computes conductance across a device between contacts at different thermal equilibria [45]. However, vibrations in the device cannot thermalize and reach a steady-state non-equilibrium distribution due to the harmonic assumption. Once phonons leak to the contacts, implicit scattering processes take them to equilibrium, creating a resistance at the two interfaces of the device and contacts [45]. These resistances can be approximated defining an artificial local temperature at slabs of the device along the transport direction. At each slab, the temperature is found equating its total energy, arising from a non-equilibrium distribution, to an equilibrium distribution [51]. A temperature profile versus position of one of our interfaces, converting local non-equilibrium energy to equilibrium distributions, has three temperature drops: one at each contact-device boundary and one at the GaN-sAlN interface that we are modeling (see Figure 3b of reference [52] for an example). In the data extracted from measurements there is only a single temperature drop at the GaN-sAlN interface. The conductance at the GaN contact can be approximated as twice the conductance of a homogeneous material G_{GaN} [45,52]

$$G_{GaN} = \frac{1}{A}\int_0^\infty \frac{d\omega}{2\pi} C(\omega) M_{GaN}(\omega) \quad (5)$$

since transmission is unity across a device composed of a homogeneous system, and the temperature drops are equal and localized to the two contact-device boundaries. Thus, the conductance of each boundary is twice that of G_{GaN}. A similar definition is valid for the resistance at the sAlN contact. Using Eq. 5 and assuming that the total resistance is the sum of resistances at the contacts plus resistance at the GaN-sAlN interface, we can approximate the interface conductance without contact resistance as [52]

$$G' = \frac{G}{1 - G\left(\frac{1}{2G_{GaN}} + \frac{1}{2G_{AlN}}\right)} \quad (6)$$

Note that the same equation was derived from arguments of local equilibrium related to four-point probe measurements [31]. Figure 2b demonstrates that excluding the contact resistance for the type 1 and type 2 interfaces results in a 22% increase of conductance (dashed curves). Although this does not fully explain the discrepancy between theory and experiments, it is a sizable effect that should be considered in future first-principles calculations of *G*. A better description of this phenomena requires further understanding of phonon thermalization at interfaces.

The wave nature of phonons interacting with interfaces in close proximity, like those of the 4nm sAlN layer in experiments, may also bridge the gap between theory and experiments. The resistance across two identical interfaces close to each other can be smaller than the sum of resistances of the interfaces in isolation due to tunneling and interference [47]. To obtain an upper bound of possible wave effects resulting from phonons crossing close interfaces, *G* was calculated for a GaN-sAlN-GaN double interface setting the thickness of the sAlN layer to 3.906 nm (Figure 2a). The IFCs at each interface are the same as those from the single type 1 and type 2 interfaces used in Figure 2b, while the IFCs of the sAlN unit cells joining them come from bulk sAlN. Figure 2c shows *G* of the double interface with and without contact resistance. It is compared with the conductance determined from the measured κ_{SL} using $1/G$ instead of $2/G$ in Eq. 4 to extract the conductance of the double interface. While the experimental data halves from Figure 2b to Figure 2c, the NEGF conductance does not, reducing the discrepancy with the measured data from 45% to 25% at room temperature (using the values without contact resistance). $MT(\omega)$ for the double interface is compared with that of single interfaces in Figure 2d.

Interatomic mixing and anharmonicity at the interface are also important factors that these harmonic *G* calculations neglect. Ironically, adding interfacial disorder to a perfectly abrupt interface can *increase G*. The disorder breaks symmetry parallel to the interface allowing transmission between phonons with different components of momentum perpendicular to the interface. G increases if these new transport channels are larger than the backscattering induced by disorder [32]. Molecular dynamics, as well as NEGF simulations, have shown that adding interatomic mixing to an otherwise perfect interface enhances *G* by 10 to 20% [31,32,53], a non-negligible effect. However, those simulations only included the effect of disorder through mass variance. Other simulations on interfaces with larger amounts of intermixing and atomic

rearrangement, that accounted for mass and IFC variance using empirical potentials, predict the opposite effect [54]. As the effect of IFC variance from interfacial disorder has not been considered from first-principles, its impact on *G* remains unclear. Anharmonicity can also enhance interfacial thermal conductance as it allows phonons to thermalize near the interfaces favoring states with higher transmission [55–59]. An increase of interfacial conductance with temperature is commonly seen in molecular dynamics simulations [59,60]. Recently this enhancement was captured by a NEGF methodology combining Büttiker probes with phenomenological scattering rates [37]. A fully first-principles treatment of *G* including anharmonic IFCs from first-principles near the interface has not been done. These represent future challenges for this field of research.

IV. SENSITIVITY TO SUPERCELL GEOMETRY AND RELAXATION

Supercell geometry: Interfacial supercells (Figure 1c) should be large enough to capture the evolution of IFCs from one bulk material on one side of the interface to the other. An ideal set of IFCs would automatically capture long-range interactions and satisfy all invariances (point group, derivative permutation, translational and rotational). However, realistic numerical simulations are limited to fairly small size and thus interfacial IFCs can vary according to how supercells are constructed (W, L_{cell}, and L_{cut} in Figure 1). Sensitivity of the calculated interfacial conductance to variances of the IFCs from different supercell structures are examined here.

To simplify the analysis, the temperature dependence of *G* (Eq. 1) is removed by taking the high temperature limit of the mode heat capacities

$$G_\infty = \frac{k_B}{2\pi A}\int_0^\infty d\omega MT(\omega) \tag{7}$$

Under this approximation all available frequencies contribute to transport and conductance is proportional to the area under $MT(\omega)$. Also, the contributions from the high frequency optic phonons (G_∞^{Op}, above the bandgap in Figure 2d) and lower frequency optic and acoustic modes (G_∞^{Ac}, below the bandgap) are distinguished, $G_\infty = G_\infty^{Ac} + G_\infty^{Op}$.

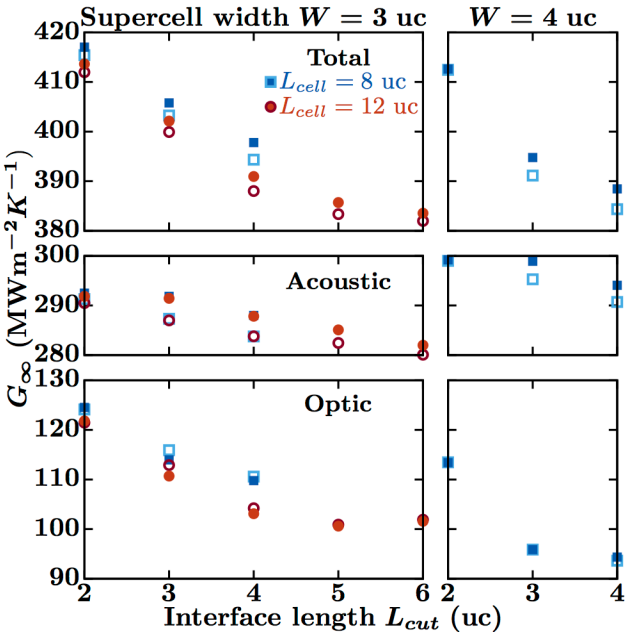

Figure 3: High temperature conductance versus the number of unit cells in the interface L_{cut} for supercells with W=3 uc (left) and 4 uc (right), and L_{cell} =8 uc (blue) and L_{cell}=12 uc (red). Solid symbols use IFC sets with space group, permutation, translational and rotational invariances enforced, while open symbols use IFC sets with only space group and permutation invariances enforced. At $L_{cut} = 6$ uc, interface conductance is nearly converged with respect to L_{cut}.

Interfacial IFCs are extracted from a 432-atom ($W = 3$ uc, $L_{cell} = 12$) supercell (Figure 1) and the cutoff length L_{cut} defining the IFCs used in the device is varied from 2 to 6 uc. Convergence of *G* with respect to L_{cut} is nearly achieved by $L_{cut} = 6$ uc as shown by the open red circles in Figure 3, which are derived from IFC sets satisfying only space group and derivative permutation invariances. The conductance trend is primarily dictated by changes in G_∞^{Op} resulting from the inclusion of longer-range IFCs with increasing L_{cut} for these polar systems (Figure 3). From $L_{cut} = 5$ to $L_{cut} = 6$ uc, G_∞ decreases by less than 0.4%, G_∞^{Op} plateaus at about 102 MWm^{-2}K^{-1} and G_∞^{Ac} decreases by less than 0.9%. Despite the relatively small variance, G_∞^{Ac} does not seem to plateau with increasing L_{cut}. Analyzing the convergence of our transport calculations merely based on conductance might be misleading as G_∞ is proportional to the area under $MT(\omega)$; it is an integrated quantity with no spectral information. For our case, $MT(\omega)$ for L_{cut}=4, 5 and 6 uc are very similar (Figure 4) and the difference between integrated $MT(\omega)$ values ($\int d\omega \left| MT_{L_{cut}=i+1}(\omega) - MT_{L_{cut}=i}(\omega) \right|$) for consecutive L_{cut} decreases as L_{cut} increases. More importantly, the differences for these values for frequencies below the bandgap tends to zero, suggesting that G_∞^{Ac} is nearly converged. Similar convergence trends for G_∞, G_∞^{Op} and G_∞^{Ac} are obtained when translational and rotational invariances are enforced on the IFCs (solid red dots in Figure 3).

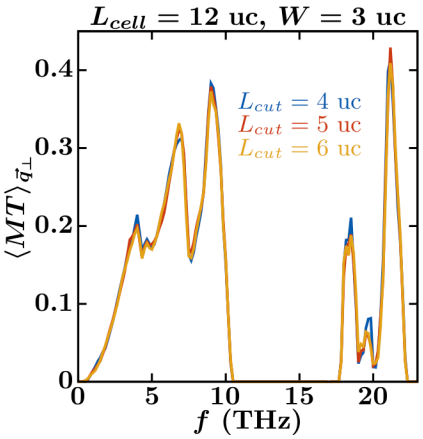

Figure 4: (a) Average $MT(\omega)$ per simulation cell for different interface cutoff lengths L_{cut} corresponding to open red circles in Figure 3. The similarity of the curves demonstrates that $MT(\omega)$ is close to a converged value by $L_{cut} = 6$ uc.

To complement the study on interface cutoff length dependence, we also examined $MT(\omega)$ and G_∞ with different supercell constructions: 288-atom ($L_{cell} = 8, W = 3$) and 512-atom ($L_{cell} = 8, W = 4$) supercells with varying L_{cut}. Blue open squares in Figure 3 give G_∞ versus L_{cut} demonstrating an approach to convergence by $L_{cut} = 4$ uc. We conjecture that the conductance for a $L_{cut} = 6$ uc interface from a $W = 4$ uc and $L_{cell} = 12$ uc supercell should be about 3% lower than $G_\infty = 384.35$ MWm^{-2}K^{-1}, the value from a supercell with $L_{cell} = 8$ uc, $W = 4$ uc and $L_{cut} = 4$ uc. This expectation is based on our calculations using IFCs from supercells with $W = 3$ (Figure 3). Note that the change in G_∞ when increasing the supercell size is mostly due to the optical phonon spectrum, while G_∞^{Ac} remains unchanged (see Figure 3 for $L_{cell} = 8$ uc and $L_{cell} = 12$ uc when $W = 3$ uc).

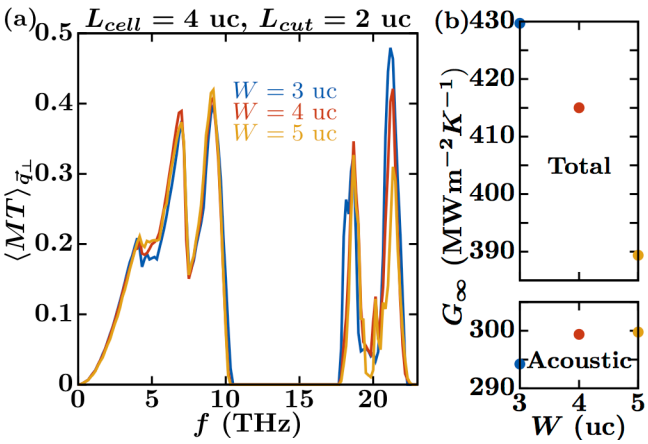

Figure 5: (a) Average $MT(\omega)$ per simulation cell and (b) G_∞ for systems whose interfacial IFCs are computed from supercells with various widths W (Figure 1). At $W = 5$ uc, G_∞^{Op} has not converged due to the truncation of the long-range IFCs that give rise to LO-TO splitting.

Evaluating sensitivity of G to the cross-section W of the interfacial supercell (Figure 1c) is more challenging since the number of atoms scales as W^2. For $L_{cell} = 12$ uc with $W = 4$ and 5 uc, the supercell atom count rises from 768 to 1200, respectively, both systems beyond typical numerical budgets given the large memory and processing constraints. To circumvent this problem, the interfacial cutoff length is reduced to $L_{cut} = 2$ uc with $L_{cell} = 4$ uc to test the interfacial conductance sensitivity to supercell width (see Figure 5). While G_{∞}^{Ac} and the acoustic contributions to $MT(\omega)$ are close to convergence at $W = 5$ uc, G_{∞}^{Op} is not. $MT(\omega)$ decreases notably over the optical frequency spectrum, precisely where our FD IFCs do not capture the LO-TO splitting well (Figure 15). This well-known problem for real-space calculations of IFCs for polar materials could be ameliorated using a correction for the neglected non-analytic contributions [61], which is not trivial for these calculations.

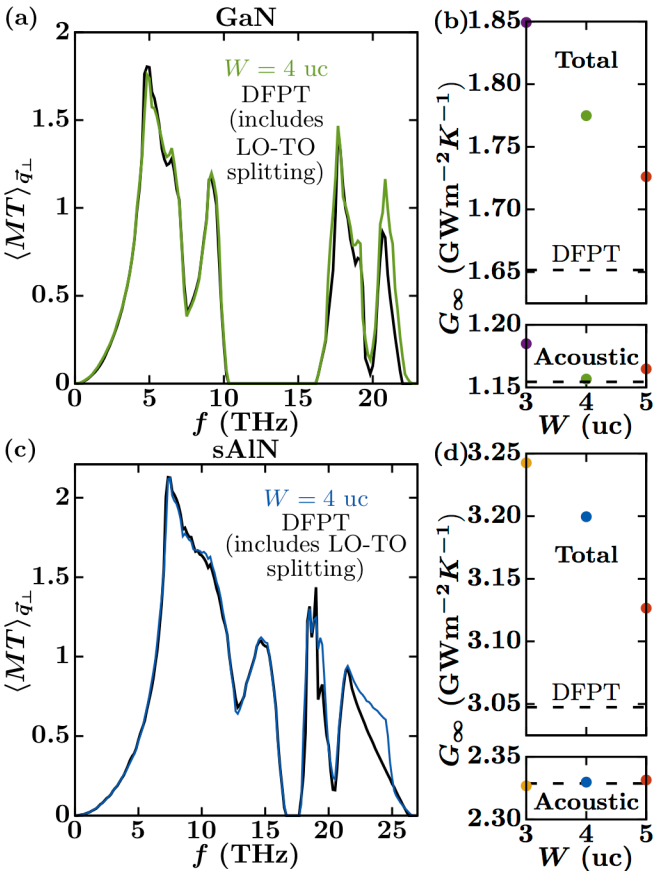

Figure 6: Average $MT(\omega) = M(\omega)$ per simulation cell and G_∞ for bulk GaN ((a) and (b), respectively) and sAlN ((c) and (d), respectively) using IFCs determined from the finite displacement (FD) method on $W \times W \times W$ supercells versus those calculated from density functional perturbation theory (DFPT). DFPT IFCs include long-range, non-analytical corrections and capture LO-TO splitting.

The uncertainty of calculations of $MT(\omega)$ and G_∞ with relation to neglecting long-range, non-analytical IFCs is estimated via calculations of these for bulk GaN and sAlN, for which these long-range interactions can be included. For bulk materials, phonon transmission is unity and $MT(\omega) = M(\omega)$. Besides using Eq. 2 on bulk crystals, $M(\omega)$ can be computed in a more intuitive way. For each $\vec{q}_\perp$, the dispersion along the transport direction can be calculated and the number of bands available at each ω counted. Summing over the 2D Brillouin zone where $\vec{q}_\perp$ is defined, we determine $M(\omega)$. Doing this process with a phonon dispersion that includes non-analytical, long-range IFCs from separate density functional perturbation theory (DFPT) calculations, we determine $M(\omega)$ and G_∞ in the limit of infinite supercell size for GaN and sAlN (Figure 6). Our calculations indicate that G_∞ including LO-TO splitting is 7% and 5% lower than that obtained using FD IFCs from $4 \times 4 \times 4$ bulk supercells of GaN and sAlN, respectively. Thus, we estimate that G_∞ for an interface with IFCs coming from supercells with cross-section W tending to infinity is likely similarly lower than that from a $W = 4$ uc supercell. This estimation of lower *G* ignores the LO-TO splitting effect from sAlN because its largest changes in $M(\omega)$ occur above 22.6 THz, the maximum frequency of GaN. Thus, these modes do not contribute to G in our elastic transport calculations, which require available transport channels in both contacts to have non-zero $MT(\omega)$. $MT_{DMM}(\omega)$ in Eq. 3 can also be calculated including long-range IFCs. Figure 7 shows $MT_{DMM}(\omega)$ for both cases (with and without long-range Coulomb interactions) and highlights differences in the high frequency optical spectrum. The resulting G_∞ differ by 7.3%.

Summing up conductance sensitivity to interface cutoff length and supercell cross-section, we expect that our reported values of conductance using $L_{cell} = 8$ uc, $W = 4$ uc and $L_{cut} = 4$ uc to be 10% larger than a fully converged value. Note this error is in the limit of high temperature, where G_∞^{Ac} and G_∞^{Op} constitute 76% and 24% of the total G_∞, respectively. As temperature decreases, G_∞^{Op} decreases due to the heat capacity in Eq. 1, thus, the expected error due to neglecting LO-TO splitting decreases. For example, at room temperature G^{Op} gives 14% of G so the error decreases to 14/24*10%.

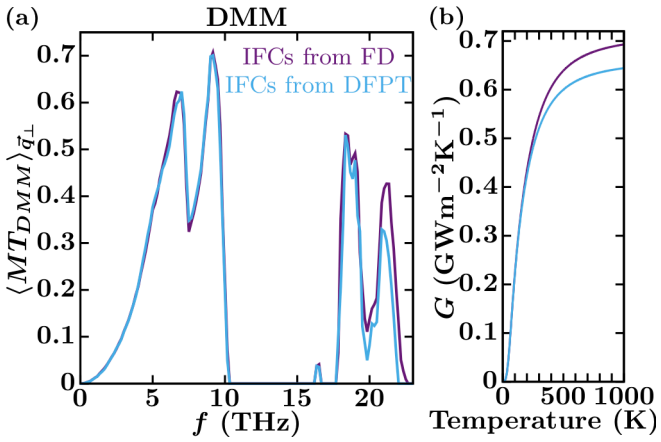

Figure 7: (a) Average $MT_{DMM}(\omega)$ per simulation cell and (b) G with and without long-range Coulomb interactions. G_∞ from DFPT is 7.3% smaller than G_∞ from FD.

Again, the interfacial IFCs were extracted from $W \times W \times L_{cell}$ supercells with a single interface (Figure 1c). Using these IFCs to create the phonon dispersion of a superlattice (not used directly in the NEGF methodology) gives an imaginary longitudinal acoustic branch along the Γ to A direction (plotted as a negative blue branch in Figure 8a). This imaginary branch does not affect our NEGF interface conductance calculations. When including three interfaces in the supercell (doubling the supercell size and explicitly constructing superlattice periodicity), while keeping the same $W = 3$ and $L_{cell} = 4$, eliminates this imaginary branch (see Figure 8a). An instability near the Γ point re-emerges when explicitly including five interfaces in the supercell (triple the original supercell size). Note that these 'superlattice' constructions should be equivalent, however, Figure 8a demonstrates differences in the dispersions. Despite these differences, their associated interface conductance calculated from NEGF are similar. The acoustic contributions to $MT(\omega)$ (Figure 8b) are almost independent of the number of interfaces included in the supercell and G_∞^{Ac} varies by less than 0.7% (Figure 8c). Changes in G_∞^{Op} arise from longer atomic interactions and should converge as the number of interfaces in the supercell increases. This analysis is relevant to calculation of IFCs by finite displacements as smaller supercells (higher computational efficiency) that give physically-meaningful results are desired.

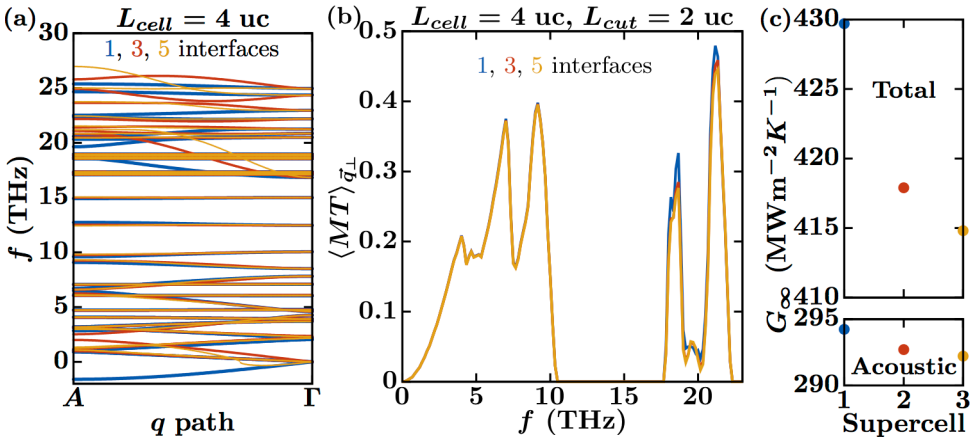

Figure 8: (a) Phonon dispersions for supercells with increasing number of interfaces (one, three and five) while keeping $W = 3$ uc and $L_{cell} = 4$ uc constant. Single interface (b) Average $MT(\omega)$ per simulation cell and (c) G_∞ using interfacial IFCs from these systems. Despite the different low frequency phonon behavior, $MT(\omega)$s are nearly identical below 5 THz, suggesting the imaginary phonon frequencies from the single interface supercells do not affect the NEGF transport calculations.

Supercell relaxation: Despite the variations of calculated IFCs that accompany atomic relaxation, we find negligible sensitivity of G with the quality of relaxation. IFCs from $W = 5$ uc supercells built using $L_{cell} = 4$ uc interface cells were determined in four different ways: (1) Atomic positions for an interface cell were relaxed until interatomic forces were < 7.8×10^{-7} Ry Bohr^{-1}. Then the supercell was built and IFCs were calculated without further atomic relaxation. At this point, atomic forces on the supercell were less than 2.4×10^{-4} Ry Bohr^{-1}. (2) Calculation similar to (1) but atomic positions on the supercell were further relaxed with <4.2×10^{-5} Ry Bohr^{-1} precision. (3) Calculation similar to (1) but the strict initial relaxation bound on the interatomic forces of the interface cell is loosened to 4.9×10^{-5} Ry Bohr^{-1}. (4) The primitive unit cells along the supercell (z direction) were compressed by 0.075% (~0.015 Å) and atomic positions were relaxed until interatomic forces <8.3×10^{-5} Ry Bohr^{-1}. The calculated $MT(\omega)$ values for all systems are similar and the variance of G among them is less than 0.16% (Figure 9). From these results we learn that calculations of IFCs, $MT(\omega)$ and G are insensitive to small variances in atomic positions and stringent relaxations, within reason, are not required.

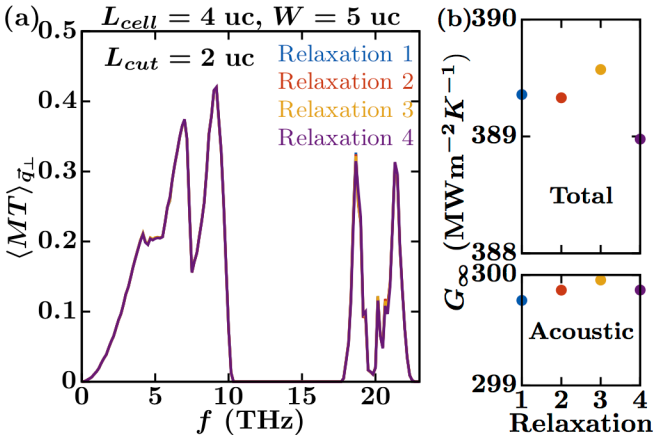

Figure 9: (a) Average $MT(\omega)$ per simulation cell and (b) G_∞ for systems whose IFCs are determined with different levels of atomic relaxation of the supercells.

V. SENSITIVITY TO INVARIANCE CONDITIONS

Numerically calculated IFCs from finite supercells typically violate invariance constraints of the physical system (point group (PG), derivative permutation (DP), translational (TI) and rotational (RI) invariances) [62–64]. Furthermore, such invariances are broken when combining the non-periodic interface cell with the bulk contacts. In this section, sensitivity of the calculated interfacial conductance to variances of the IFCs from different applications of the invariance constraints are examined.

For analysis here, we consider the interfacial system $L_{cell} = 8$ uc, $W = 4$ uc and $L_{cut} = 4$ uc because results from this configuration were compared with measurements in Figure 2. Detailed results for some other systems are shown in Figure 3 and Figure 11. Enforcing DP guarantees that the IFC matrix of the system is symmetric and avoids instabilities or negative values of $MT(\omega)$ (Figure 10a). Aside from a few instabilities, $MT(\omega)$ calculated from the IFC set before enforcing any invariance constraints ('None') is almost identical to that from a set where DP was enforced (Figure 10a). Additional enforcement of SG also results in a very similar $MT(\omega)$ (Figure 10a). Figure 10b compares calculations of $MT(\omega)$ from IFCs with DP and SG enforced with that from IFCs where TI and RI are also enforced by changing the least possible all irreducible IFCs (details in Appendix A). This process only changes $MT(\omega)$ slightly at low frequencies and does not alter phonon transmission properties above 6 THz (Figure 10b and G_∞^{Op} in Figure 11). Note G_∞ from enforcing DP, SG, TI vs. enforcing DP, SG, TI, RI differ by less than 2%, however, differences become larger as L_{cut} and W decrease (Figure 11).

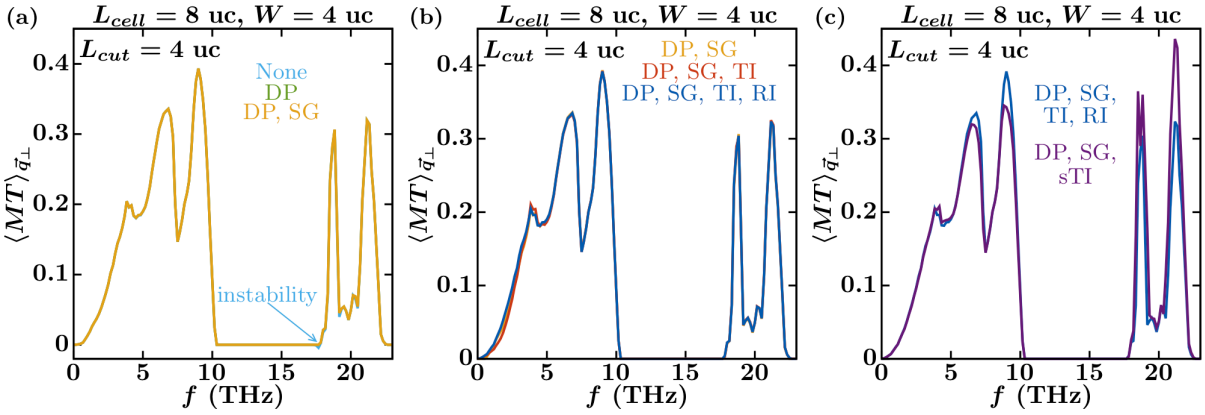

Figure 10: Average $MT(\omega)$ per simulation cell from IFCs that satisfy different symmetry invariances. (a) Comparison of $MT(\omega)$ for IFCs directly from FD calculations ('None'), when enforcing derivative permutation (DP) and when enforcing DP and space group (SG) symmetries. (b) $MT(\omega)$ for IFCs with DP and SG compared to these with the addition of enforcing translational (TI) and rotational (RI) invariances, while minimizing the change in IFCs with DP and SG. (c) Enforcing simple translational invariance (sTI), commonly known as the simple acoustic sum rule, generates visible changes in $MT(\omega)$ that result in a 7% overestimation of G_∞.

A more commonly used method to enforce TI consists of equating onsite IFC matrix elements to the negative of the sum of all IFC matrices originating from that site, which is known as the simple acoustic sum rule (sTI). This process is simple to implement, but usually breaks DP and SG symmetries. Figure 10c compares $MT(\omega)$ from IFC sets where TI and RI are enforced with those where sTI invariances are enforced. Transport properties are notably changed above 6 THz when using the sTI (Figure 10b and c). This results in a 35% (6%) overestimation of G_∞^{Op} (G_∞) and a 3.5% underestimation of G_∞^{Ac} compared to the other sets (Figure 11a). Below 3.5 THz using sTI and TI+RI yield similar $MT(\omega)$, so sTI may still be useful in low temperature calculations. The differences between G_∞^{Op} from IFCs satisfying TI+RI and those satisfying sTI grow larger as L_{cut} increases and as W decreases (Figure 11). Larger L_{cut} implies more onsite IFC matrices are modified, allowing for more distribution of variations, while shorter W gives fewer IFC matrices, so changes of the onsite terms are more noticeable.

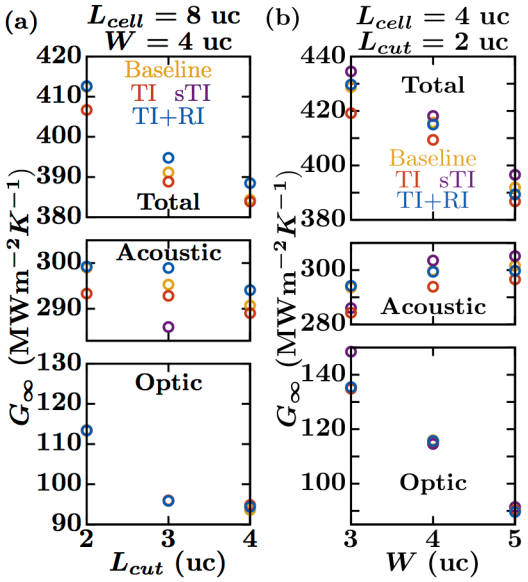

Figure 11: G_∞ resulting from IFCs that satisfy various invariances as (a) the truncation length L_{cut} and (b) the supercell width W vary.

VI. COMPARISON WITH OTHER APPROXIMATIONS

Calculating interfacial IFCs from first-principles is computationally demanding, thus many approximations have been used previously to determine them from IFCs of the bulk materials. We examine some of these here; in particular, we approximate the interfacial IFCs (with $L_{cut} = 4$ uc) for four separate cases by using IFCs from (1) bulk GaN, (2) bulk sAlN, (3) the arithmetic mean (AM) of bulk GaN and sAlN, and (4) their harmonic mean (HM). The masses of the atoms were unaltered. The IFCs from these separate approximations are connected to GaN and sAlN contacts and all symmetries and invariances are enforced. All these approximations overestimate our fully first-principles G by about 13% at room temperature and up to 20% at high temperatures (see Figure 12b). G from the AM and HM calculations are similar and bounded by G using interfacial IFCs from the contacts. As expected, long wavelength phonons up to 6 THz are insensitive to the choice of interfacial IFCs and differences in $MT(\omega)$ tend to increase with phonon frequency (Figure 12a). Interestingly, G from the AM set is larger than that from the HM set contrary to predictions by simple models [46].

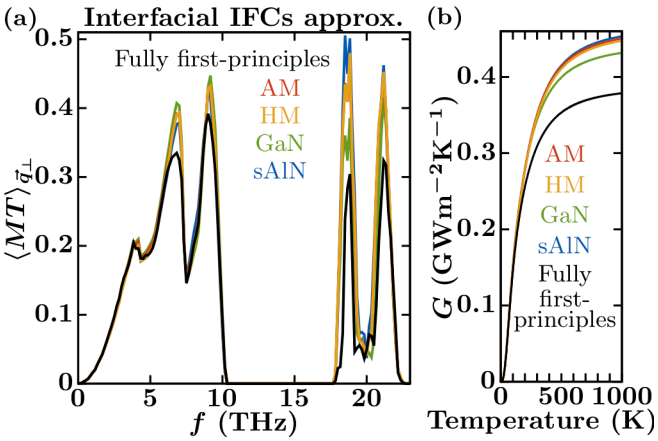

Figure 12: (a) Average $MT(\omega)$ per simulation cell and (b) G for GaN-sAlN interfaces using common approximations for the interfacial IFCs. Namely, interfacial IFCs determined from the arithmetic mean (AM) and harmonic mean (HM) of the IFCs of GaN and sAlN, as well as simply using the IFCs of pure GaN and sAlN.

Most of the existing '*ab-initio*' interface conductance simulations only include mass variance effects, using IFCs from a single bulk material and fully neglecting IFC variations at the interfaces [31–33]. To test this approximation, *G* of GaN-sAlN interfaces assuming that all the IFCs of the system are either those of GaN or sAlN are computed (Figure 13). Our calculations indicate that neglecting IFC variance overestimates the fully first-principles *G* by 15% to 60% at room temperature, with important differences over the whole frequency spectrum. Note the spectral differences in $MT(\omega)$ arise not only due to removing IFC variance at the interface but also due to changes in the phonon spectra at the contacts.

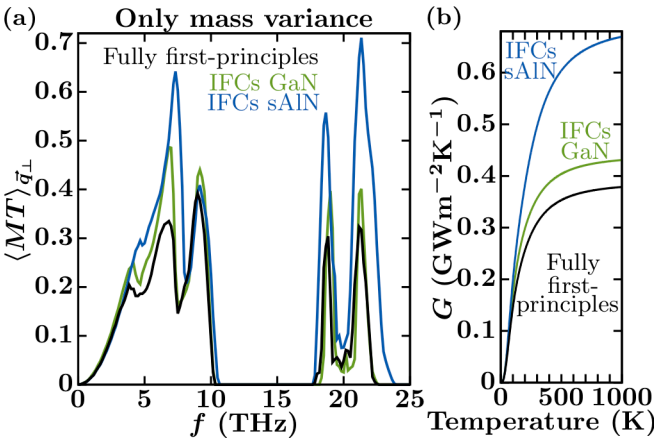

Figure 13: (a) Average $MT(\omega)$ per simulation cell and (b) *G* for GaN-sAlN interfaces considering only mass variance. The IFCs of the whole interfacial system are equated to either those of GaN (green curves) or sAlN (blue curves). These are compared to the fully first-principles calculations (black curves).

In spite of the limitations of approximating interface *G* only including mass variance effects, this variance captures better the fully first-principles *G* than when only interfacial IFC variance is

included. $MT(\omega)$ and *G* for GaN-sAlN interfaces assuming that all of the masses of the system are either those of GaN or sAlN, while keeping the IFCs equal to those from the fully first-principles calculation, are shown in Figure 14. Including only IFC variance at the interface overestimates the fully first-principles *G* by 290% to 430% at room temperature. Most of the differences arise due to the change in phonon spectra at the contacts when the Ga masses are replaced by those of Al and vice versa, which transforms the GaN-sAlN interface to an interface between materials with more similar vibrational spectra.

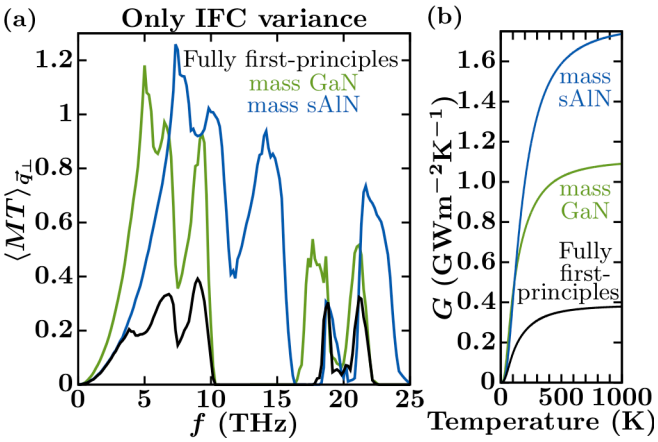

Figure 14: (a) Average $MT(\omega)$ per simulation cell and (b) *G* for GaN-sAlN interfaces considering only IFC variance. The masses of the whole interfacial system are equated to either those of GaN (green curves) or sAlN (blue curves) while the IFCs are those from the fully first-principles calculation. These are compared to the fully first-principles calculations (black curves).

VII. SUMMARY AND CONCLUSIONS

Phonon thermal conductances (*G*) of GaN-AlN interfaces were calculated using a non-equilibrium Green's function formalism in the harmonic limit with interfacial interatomic force constants (IFCs) from density functional theory. The influence of varying geometric supercell parameters, IFC symmetry constraints and relaxation methods were quantitatively assessed in terms of spectral transmission and *G*. This numerical effort provides uncertainty benchmarks for balancing computational efficiency and numerical accuracy for future interfacial calculations. Neglecting long-range interactions of these polar systems yields an estimated ~10% increase in G. Enforcing a simple acoustic sum rule for translational invariance instead of more sophisticated methods overestimates the optic contributions to G by 35%, using *ad hoc* interface IFCs, such as the arithmetic mean of bulk IFCs, overestimates G by up to 20%, and only including mass variance at the interface overestimates *G* by up to 60%. Our conductance calculated fully from first-principles in the harmonic limit is nearly two times lower than values inferred from superlattice measurements. The possible physical origins for this discrepancy

were examined in detail. In particular, neglecting anharmonicity and interfacial atomic disorder, as well as artificial contact resistance in the Green's function calculations, reduces *G*. Our work outlines guidelines for first-principles calculations of 'physically correct' interfacial IFCs and conductance in the harmonic limit. It also contributes towards developing predictive calculations and a more complete picture of thermal transport across interfaces.

VIII. ACKNOWLEDGEMENTS

C.A.P and L.L. acknowledge support from the US Department of Energy, Office of Science, Basic Energy Sciences, Material Sciences and Engineering Division and computational resources from the National Energy Research Scientific Computing Center (NERSC), a DOE Office of Science User Facility supported by the Office of Science of the U.S. Department of Energy under Contract No. DE-AC02-05CH11231.

APPENDIX A: CALCULATIONS DETAILS

Density functional theory. DFT calculations used the pw.x module of Quantum Espresso [43], a density functional theory package based on plane wave basis sets. Valence electrons are represented with projected augmented-wave pseudopotentials (Al.pz-n-kjpaw_psl.0.1.UPF, N.pz-n-kjpaw_psl.0.1.UPF, Ga.pz-dn-kjpaw_psl.0.2.UPF) [65] using the local density approximation and Perdew-Zunger parametrization [66] for exchange-correlations. The cutoff energy for the plane waves was set to 100 Ry and the energy convergence threshold was less than 10^{-11} Ry.

Atomic relaxation. Equilibrium lattice parameters (*a*, *c* and *u*) of GaN and AlN are determined using the vc-relax option and sampling the Brillouin zone with a $9 \times 9 \times 6$ Monkhorst-Pack mesh [67] displaced from the origin. The structural parameters deviate by less than 1% from measurements (Table 1). The in-plane lattice parameter (*a*) of AlN expands to match that of GaN in GaN-AlN superlattices with thin AlN layers [25]. Thus, relaxed out-of-plane lattice parameters (*c* and *u*) of strained GaN and AlN (using the relaxed *a* of the other material) were computed and given in Table 1. Combining optimized unit cells of GaN and sAlN, the primitive unit cells of GaN-sAlN supercells are built, which are referred to as interface cells (Figure 1b). The sGaN configuration is used to compute *G* for an sGaN-AlN interface for comparison with GaN-sAlN *G*. All the out-of-plane degrees of freedom (along z axis here) are relaxed using a $9 \times 9 \times 2$

Monkhorst-Pack mesh (except for supercells with $L_{cell} < 6$ uc, where a $9 \times 9 \times 3$ mesh was used) until atomic forces were less than 10^{-4} Ry Bohr^{-1}. In-plane atomic coordinates were fixed since they did not change during the initial relaxation steps and fixing them reduces the computational cost. Relaxed out-of-plane lattice parameters for supercells with various L_{cell} are shown in Table 2 and atomic positions are available in the scf input files of these systems available in the supplemental material [68].

	GaN		AlN		sGaN	sAlN
	Theory	Experiment	Theory	Experiment	Theory	Theory
a (Å)	3.1619	3.190	3.0880	3.110	3.0880	3.1619
c (Å)	5.1561	5.189	4.9427	4.980	5.2165	4.8657
u	0.3763	0.377	0.3819	0.382	0.3699	0.3894

Table 1: Equilibrium lattice parameters for GaN, AlN and their strained counterparts (sGaN and sAlN), where the in-plane lattice of GaN is set to that of AlN and vice versa. Experimental values are from Schulz et al. [69].

L_{cell}	c/L_{cell} (Å/uc)
2	5.0255
4	5.0220
6	5.0208
8	5.0201
12	5.0194

Table 2: Calculated out-of-plane lattice parameter of GaN-sAlN supercells of various lengths (L_{cell}) after atomic and volume relaxation.

Interatomic force constants: IFCs are calculated as numerical derivatives of forces from supercells with individual atoms displaced by ± 0.04 Å, the finite displacement (FD) method. Supercells are built by repeating relaxed primitive unit cells and atomic forces are determined using scf computations sampling only the Γ point of the Brillouin zone. Figure 15a and 15b show phonon dispersions of bulk GaN and AlN determined with IFCs from the FD method on $4 \times 4 \times 4$ supercells. The dispersions are in good agreement with experimental data except for the longitudinal-optic (LO) branch close to the Γ point. For polar materials, like GaN and AlN, the FD method does not capture well the splitting between the longitudinal-optic and the transverse-optic branches (LO-TO splitting) around the Γ point because it truncates long-range, non-analytical Coulomb interactions. The extent of this effect is shown in Figure 15a and 15b, depicting dispersions using IFCs from density functional perturbation theory (DFPT), which includes these interactions [61]. Increasing the size of the supercell used in the FD method is not a viable path to fix LO-TO splitting as convergence is slow (Figure 15d and 15e). The FD method is also used to determine IFCs for strained GaN and AlN (Figure 15c) and for the GaN-sAlN interfacial supercells used in this study.

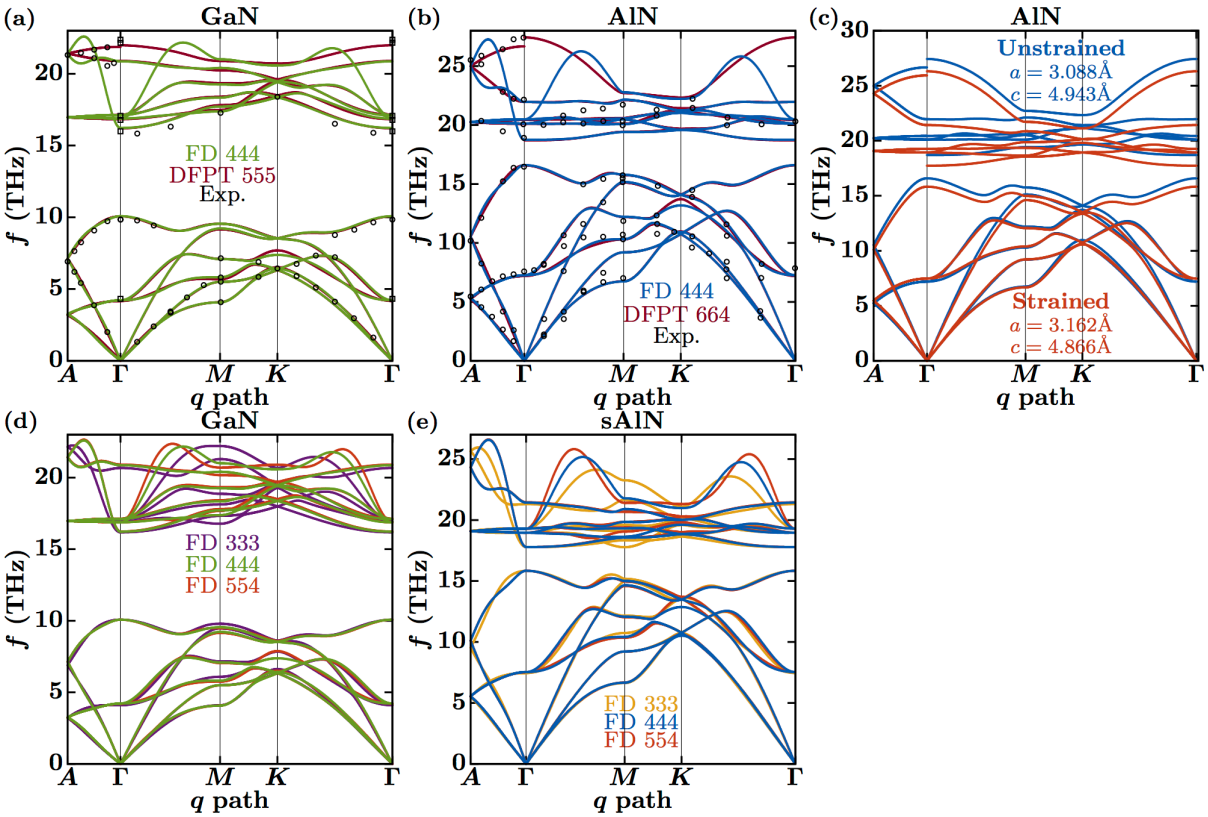

Figure 15: Phonon dispersions of (a) GaN and (b) AlN from finite displacements in a $4 \times 4 \times 4$ supercell, DFPT using $5 \times 5 \times 5$ and $6 \times 6 \times 4$ reciprocal space grids, respectively, and measured values from inelastic x-ray scattering [70,71] and Raman spectroscopy [72]. (c) Phonon dispersions of unstrained and strained AlN from DFPT. Phonon dispersions of (d) GaN and (e) sAlN from FD with varying supercell size.

Enforcing symmetry on IFCs: After obtaining IFCs from the FD method, various invariances required for 'physically correct' sets of IFCs are enforced. Space groups of the primitive unit cells are obtained using the spglib library created by Togo [73] (186 for GaN and AlN, and 156 for GaN-sAlN interfacial supercells). With the symmetry operations of each group and derivative permutation invariance, a set of irreducible IFCs is chosen. Their values are determined using singular value decomposition from the IFCs extracted from FD [62]. Then, quadratic programing is used to solve for new values of the irreducible IFCs that satisfy translational and rotational invariance subject to the constraint of minimizing the Euclidean distance to the former set of irreducible IFCs. This procedure has been previously used to enforce invariances on IFCs near defects [74,75]. Note that enforcing rotational invariance is especially important when the cross-section of the supercell is 3×3 uc^2 as it fixes some imaginary frequencies in acoustic branches close to the Γ point.

Non-equilibrium Green's functions (NEGF): The following brief description is based on reference [45], but there are other useful resources available in the literature [28,49]. Consider

an abrupt material interface in the xy plane formed joining two semi-infinite crystals along z. Treating it as a 2D crystal made of 1D chains along z, we split the dynamical matrix of the system into large enough blocks such that only first nearest neighbor blocks interact along z are non-zero. A sample block $D_{n,m}^{s,t}$ relates the degrees of freedom of the s^{th} unit cell, located at z_s on the n^{th} 1D chain with those of the t^{th} unit cell, located at z_t on the m^{th} 1D chain. Using these blocks, the 2D crystal is transformed into reciprocal space and the coupled 1D chains in real space turn into decoupled 1D chains in reciprocal space. Each reciprocal chain is labeled by a two-dimensional wavevector $\vec{q}_\perp$ in the 2D Brillouin zone and a block of its dynamical matrix relating the s^{th} and t^{th} unit cells is given by

$$D_{\vec{q}_\perp}^{s,t} = \sum_m D_{n,m}^{s,t} e^{-i\vec{q}_\perp \cdot (\vec{r}_{n\perp} - \vec{r}_{m\perp})} \tag{8}$$

with $\vec{r}_{n\perp}$ and $\vec{r}_{m\perp}$ the lattice vectors of the n^{th} and m^{th} real space 1D chains, respectively. The block tridiagonal dynamical matrix of the $\vec{q}_\perp$ reciprocal 1D chain is divided into device (D), left contact (L) and right contact (R) regions

$$D_{\vec{q}_\perp} = \begin{pmatrix} D_{\vec{q}_\perp}^{L} & D_{\vec{q}_\perp}^{LD} & 0 \\ D_{\vec{q}_\perp}^{DL} & D_{\vec{q}_\perp}^{D} & D_{\vec{q}_\perp}^{DR} \\ 0 & D_{\vec{q}_\perp}^{RD} & D_{\vec{q}_\perp}^{R} \end{pmatrix} \tag{9}$$

The device region contains a neighborhood of the interface large enough so atoms at the edges of this region are equivalent to those of bulk crystals. The contact regions contain the remining semi-infinite bulk 1D crystals and their dynamical matrix blocks are invariant along z ($D_{\vec{q}_\perp}^{s,s} = D_{\vec{q}_\perp}^{s+1,s+1}$ and $D_{\vec{q}_\perp}^{s,s+1} = D_{\vec{q}_\perp}^{s+1,s+2}$ with s labeling cells inside the contacts). Thus, we simplify the notation for dynamical matrix blocks of the left contact as $D_{\vec{q}_\perp}^{s,s} = D_{\vec{q}_\perp}^{L,on}$ and $D_{\vec{q}_\perp}^{s,s+1} = D_{\vec{q}_\perp}^{L,off}$. Similar notation applies for the right contact. The retarded Green´s function for the $\vec{q}_\perp$ reciprocal 1D chain is given by

$$G_{\vec{q}_\perp}^{r}(\omega) = \left[\omega^2 I - D_{\vec{q}_\perp}^{D} - \Sigma_{\vec{q}_\perp}^{L}(\omega) - \Sigma_{\vec{q}_\perp}^{R}(\omega)\right]^{-1} \tag{10}$$

with I the identity matrix and $\Sigma_{\vec{q}_\perp}^{\alpha}(\omega)$ the self-energy matrices of contact α. All matrices in Eq. 10 are square with dimensions equal to the number of degrees of freedom of atoms in the device region of the chain. $\Sigma_{\vec{q}_\perp}^{L}(\omega)$ and $\Sigma_{\vec{q}_\perp}^{R}(\omega)$ are zero everywhere except in the top-left block and the bottom-right block, respectively, which are given by

$$\begin{aligned} &\text{Top-left block of } \Sigma_{\vec{q}_\perp}^{L}(\omega) = \left(D_{\vec{q}_\perp}^{L,off}\right)^{\dagger} g_{\vec{q}_\perp}^{L}(\omega) D_{\vec{q}_\perp}^{L,off} \\ &\text{Bottom-right block of } \Sigma_{\vec{q}_\perp}^{R}(\omega) = D_{\vec{q}_\perp}^{R,off} g_{\vec{q}_\perp}^{R}(\omega) \left(C_{\vec{q}_\perp}^{R,off}\right)^{\dagger} \end{aligned} \tag{11}$$

where $g_{\vec{q}_\perp}^{\alpha}$ is the surface Green's function of contact α

$$\begin{aligned} g_{\vec{q}_\perp}^{L}(\omega) &= \left[\omega^2 I - D_{\vec{q}_\perp}^{L,on} + i\eta\omega - \left(D_{\vec{q}_\perp}^{L,off}\right)^{\dagger} g_{\vec{q}_\perp}^{L}(\omega) D_{\vec{q}_\perp}^{L,off}\right]^{-1} \\ g_{\vec{q}_\perp}^{R}(\omega) &= \left[\omega^2 I - D_{\vec{q}_\perp}^{Ro,n} + i\eta\omega - D_{\vec{q}_\perp}^{R,off} g_{\vec{q}_\perp}^{R}(\omega) \left(D_{\vec{q}_\perp}^{R,off}\right)^{\dagger}\right]^{-1} \end{aligned} \tag{12}$$

$\eta = 100$ rad s^{-1} in our calculations ensures causality. The result of Eq. 12 is independent of the precise value of η as $\eta\omega$ is infinitesimal ($\sim 10^{14}$ rad^2 s^{-2}) compared to typical dynamical matrix entries ($\sim 10^{23}$ to 10^{27} rad^2 s^{-2}). The surface Green's functions for our calculations are obtained

using a recursive algorithm described in detail in references [76,77]. The broadening matrices of the contacts are given by

$$\Gamma^{\alpha}_{\vec{q}_\perp}(\omega) = i\left[\Sigma^{\alpha}_{\vec{q}_\perp}(\omega) - \left(\Sigma^{\alpha}_{\vec{q}_\perp}(\omega)\right)^{\dagger}\right] \tag{13}$$

From Eq. 10 and 15, we get the ingredients necessary to calculate $MT(\omega)$ from Eq. 2.

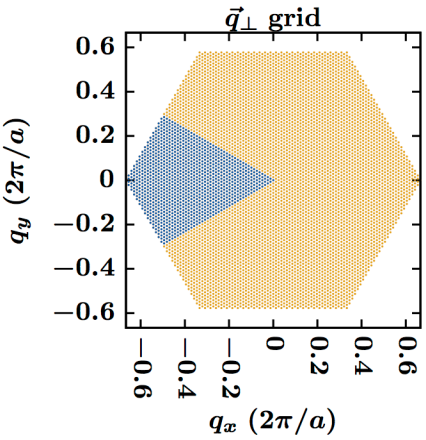

Figure 16: Full and reduced mesh in the transverse Brillouin zone used in NEGF calculations.

For our NEGF calculations, the frequency grid was formed splitting the interval 0 to 28 THz into $N_\omega = 169$ grid points. The Brillouin zone in the transverse direction was split into 6643 points with variable weights to account for a $N_{\vec{q}_\perp} = 81 \times 81$ mesh. When symmetry is enforced, we use a reduced mesh containing 1148 grid points (see Figure 16) to decrease the numerical effort. These numerical settings are well converged as doubling either the frequency or Brillouin zone grid change the conductance by less than 0.16% (see Table 3).

N_ω	$N_{\vec{q}_\perp}$	G_∞(MWm^{-2}K^{-1})
85	81×81	397.4481
169	81×81	397.7795
337	81×81	397.4496
169	41×41	396.4781
169	81×81	397.7795
169	161×161	397.1686

Table 3 High temperature conductance versus grid size in NEGF calculations.

APPENDIX B: FITTING THERMAL CONDUCTIVITY OF GaN AND AlN

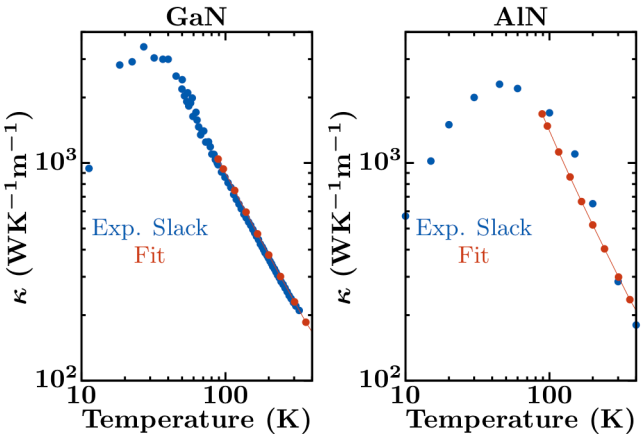

Figure 17: Thermal conductivity of GaN and AlN. Blue dots are experimental data from [78,79]

We fit experimental data combining phenomenological expressions of phonon scattering rates with vibrational frequencies and group velocities from DFPT. Thermal conductivity is computed from

$$\kappa = \sum_{\vec{q},j} \hbar\omega_{\vec{q},j} C(\omega_{\vec{q},j}) v^2_{\vec{q},j,z} \tau_{\vec{q},j}$$

with $\vec{q}$ the phonon wave-vector varying over the first Brillouin zone, j the branch index, $v_{\vec{q},j,z}$ the group velocity in z and $\tau_{\vec{q},j}$ the scattering time, which is calculated from Matthiessen's rule

$$\frac{1}{\tau_{\vec{q},j}} = \frac{1}{\tau^b_{\vec{q},j}} + \frac{1}{\tau^{ph}_{\vec{q},j}}$$

including only boundary scattering on a system with length L

$$\frac{1}{\tau^b_{\vec{q},j}} = \frac{2\left|v_{\vec{q},j,z}\right|}{L}$$

and phonon-phonon scattering

$$\frac{1}{\tau^{ph}_{\vec{q},j}} = CT\omega^2_{\vec{q},j} e^{-D/T}$$

With C and D fitting constants. The frequencies and group velocities were calculated from DFPT IFCs and $L = 500$ µm. For GaN C=1.17e-19 K^{-1}s and D=85 K while for AlN C=1.4e-19 K^{-1}s and D=200 K. Calculated conductivity values were used to extract *G* from the superlattice experiments [25].

REFERENCES

[1] D. A. Broido, M. Malorny, G. Birner, N. Mingo, and D. A. Stewart, Appl. Phys. Lett. **91**, 231922 (2007).

[2] W. Li, J. Carrete, N. A. Katcho, and N. Mingo, Comput. Phys. Commun. **185**, 1747 (2014).

[3] N. Mingo, D. A. Stewart, D. A. Broido, L. Lindsay, and W. Li, in *Length-Scale Depend. Phonon Interact.*, edited by S. L. Shindé and G. P. Srivastava (Springer New York, New York, NY, 2014), pp. 137--173.

[4] T. Tadano, Y. Gohda, and S. Tsuneyuki, J. Phys. Condens. Matter **26**, 225402 (2014).

[5] A. Togo and I. Tanaka, Scr. Mater. **108**, 1 (2015).

[6] A. Chernatynskiy and S. R. Phillpot, Comput. Phys. Commun. **192**, 196 (2015).

[7] J. Carrete, B. Vermeersch, A. Katre, A. van Roekeghem, T. Wang, G. K. H. Madsen, and N. Mingo, Comput. Phys. Commun. **220**, 351 (2017).

[8] L. R. Lindsay and C. A. Polanco, *Thermal Transport by First-Principles Anharmonic Lattice Dynamics* (Springer Nature,Cham,Switzerland, United States, 2018).

[9] L. Lindsay, D. A. Broido, and T. L. Reinecke, Phys. Rev. Lett. **111**, 025901 (2013).

[10] J. S. Kang, M. Li, H. Wu, H. Nguyen, and Y. Hu, Science (80-.). **361**, 575 (2018).

[11] S. Li, Q. Zheng, Y. Lv, X. Liu, X. Wang, P. Y. Huang, D. G. Cahill, and B. Lv, Science (80-.). **361**, 579 (2018).

[12] F. Tian, B. Song, X. Chen, N. K. Ravichandran, Y. Lv, K. Chen, S. Sullivan, J. Kim, Y. Zhou, T.-H. Liu, M. Goni, Z. Ding, J. Sun, G. A. G. U. Gamage, H. Sun, H. Ziyaee, S. Huyan, L. Deng, J. Zhou, A. J. Schmidt, S. Chen, C.-W. Chu, P. Y. Huang, D. Broido, L. Shi, G. Chen, and Z. Ren, Science (80-.). **361**, 582 (2018).

[13] A. Seko, A. Togo, H. Hayashi, K. Tsuda, L. Chaput, and I. Tanaka, Phys. Rev. Lett. **115**, 205901 (2015).

[14] J. Carrete, W. Li, N. Mingo, S. Wang, and S. Curtarolo, Phys. Rev. X **4**, 11019 (2014).

[15] L. Lindsay, D. A. Broido, and N. Mingo, Phys. Rev. B **82**, 115427 (2010).

[16] S. Mukhopadhyay, L. Lindsay, and D. S. Parker, Phys. Rev. B **93**, 224301 (2016).

[17] P. E. Hopkins, ISRN Mech. Eng. **2013**, 682586 (2013).

[18] D. G. Cahill, Rev. Sci. Instrum. **75**, 5119 (2004).

[19] R. J. Stoner and H. J. Maris, Phys. Rev. B **48**, 16373 (1993).

[20] R. M. Costescu, M. A. Wall, and D. G. Cahill, Phys. Rev. B **67**, 054302 (2003).

[21] D. Liu, R. Xie, N. Yang, B. Li, and J. T. L. Thong, Nano Lett. **14**, 806 (2014).

[22] R. B. Wilson, B. A. Apgar, W.-P. Hsieh, L. W. Martin, and D. G. Cahill, Phys. Rev. B **91**, 115414 (2015).

[23] N. Ye, J. P. Feser, S. Sadasivam, T. S. Fisher, T. Wang, C. Ni, and A. Janotti, Phys. Rev. B **95**, 085430 (2017).

[24] J. T. Gaskins, G. Kotsonis, A. Giri, S. Ju, A. Rohskopf, Y. Wang, T. Bai, E. Sachet, C. T. Shelton, Z. Liu, Z. Cheng, B. Foley, S. Graham, T. Luo, A. Henry, M. S. Goorsky, J. Shiomi,

J.-P. Maria, and P. E. Hopkins, Nano Lett. **18**, 7469 (2018).
[25] K. Y. Kan, C. Yu, D. G. Cahill, and J. Debdeep, Adv. Funct. Mater. **19**, 610 (2009).
[26] R. Cheaito, C. A. Polanco, S. Addamane, J. Zhang, A. W. Ghosh, G. Balakrishnan, and P. E. Hopkins, Phys. Rev. B **97**, 085306 (2018).
[27] N. Mingo, Phys. Rev. B **74**, 125402 (2006).
[28] J.-S. Wang, J. Wang, and J. T. Lü, Eur. Phys. J. B **62**, 381 (2008).
[29] K. Miao, S. Sadasivam, J. Charles, G. Klimeck, T. S. Fisher, and T. Kubis, Appl. Phys. Lett. **108**, 113107 (2016).
[30] S. Sadasivam, U. V Waghmare, and T. S. Fisher, Phys. Rev. B **96**, 174302 (2017).
[31] Z. Tian, K. Esfarjani, and G. Chen, Phys. Rev. B **86**, 235304 (2012).
[32] C. A. Polanco, R. Rastgarkafshgarkolaei, J. Zhang, N. Q. Le, P. M. Norris, P. E. Hopkins, and A. W. Ghosh, Phys. Rev. B **92**, 144302 (2015).
[33] B. Latour, N. Shulumba, and A. J. Minnich, Phys. Rev. B **96**, 104310 (2017).
[34] Z. Huang, T. Fisher, and J. Murthy, J. Appl. Phys. **109**, 74305 (2011).
[35] J. Zhang, C. A. Polanco, and A. W. Ghosh, J. Heat Transfer **140**, 92405 (2018).
[36] Y. Tao, C. Liu, J. Yang, K. Bi, W. Chen, and Y. Chen, in *ASME 2016 5th Int. Conf. Micro/Nanoscale Heat Mass Transf.* (2016), p. V001T03A002.
[37] S. Sadasivam, N. Ye, J. P. Feser, J. Charles, K. Miao, T. Kubis, and T. S. Fisher, Phys. Rev. B **95**, 085310 (2017).
[38] Y. Cao and D. Jena, Appl. Phys. Lett. **90**, 182112 (2007).
[39] X. Hu, J. Deng, N. Pala, R. Gaska, M. S. Shur, C. Q. Chen, J. Yang, G. Simin, M. A. Khan, J. C. Rojo, and L. J. Schowalter, Appl. Phys. Lett. **82**, 1299 (2003).
[40] A. Grier, A. Valavanis, C. Edmunds, J. Shao, J. D. Cooper, G. Gardner, M. J. Mantra, O. Malis, D. Indjin, Z. Ikonic, and P. Harrison, in *2016 IEEE Photonics Soc. Summer Top. Meet. Ser.* (2016), pp. 90–91.
[41] J. Kioseoglou, E. Kalesaki, L. Lymperakis, G. P. Dimitrakopulos, P. Komninou, and T. Karakostas, Phys. Status Solidi **206**, 1892 (2009).
[42] E. Sarigiannidou, E. Monroy, N. Gogneau, G. Radtke, P. Bayle-Guillemaud, E. Bellet-Amalric, B. Daudin, and J. L. Rouvière, Semicond. Sci. Technol. **21**, 612 (2006).
[43] P. Giannozzi, S. Baroni, N. Bonini, M. Calandra, R. Car, C. Cavazzoni, D. Ceresoli, G. L. Chiarotti, M. Cococcioni, I. Dabo, A. D. Corso, S. de Gironcoli, S. Fabris, G. Fratesi, R. Gebauer, U. Gerstmann, C. Gougoussis, A. Kokalj, M. Lazzeri, L. Martin-Samos, N. Marzari, F. Mauri, R. Mazzarello, S. Paolini, A. Pasquarello, L. Paulatto, C. Sbraccia, S. Scandolo, G. Sclauzero, A. P. Seitsonen, A. Smogunov, P. Umari, and R. M. Wentzcovitch, J. Phys. Condens. Matter **21**, 395502 (2009).
[44] C. Jeong, S. Datta, and M. Lundstrom, J. Appl. Phys. **111**, 93708 (2012).
[45] S. Datta, *Quantum Transport Atom to Transistor*, 2nd ed. (Cambridge University Press, New York, NY, 2005).
[46] C. A. Polanco, C. B. Saltonstall, P. M. Norris, P. E. Hopkins, and A. W. Ghosh, Nanoscale Microscale Thermophys. Eng. **17**, 263 (2013).
[47] C. A. Polanco and A. W. Ghosh, J. Appl. Phys. **116**, 083503 (2014).
[48] N. Mingo and L. Yang, Phys. Rev. B **68**, 245406 (2003).
[49] W. Zhang, T. S. Fisher, and N. Mingo, J. Heat Transfer **129**, 483 (2006).
[50] B. Latour, S. Volz, and Y. Chalopin, Phys. Rev. B **90**, 014307 (2014).

[51] G. Chen, *Nanoscale Energy Transport and Conversion* (Oxford University Press, New York, NY, 2005).
[52] C. A. Polanco, R. Rastgarkafshgarkolaei, J. Zhang, N. Q. Le, P. M. Norris, and A. W. Ghosh, Phys. Rev. B **95**, 195303 (2017).
[53] T. S. English, J. C. Duda, J. L. Smoyer, D. A. Jordan, P. M. Norris, and L. V Zhigilei, Phys. Rev. B **85**, 035438 (2012).
[54] X. Li and R. Yang, Phys. Rev. B **86**, 054305 (2012).
[55] E. S. Landry and A. J. H. McGaughey, Phys. Rev. B **80**, 165304 (2009).
[56] P. E. Hopkins, J. Appl. Phys. **106**, 13528 (2009).
[57] P. E. Hopkins, J. C. Duda, and P. M. Norris, J. Heat Transfer **133**, 62401 (2011).
[58] K. Sääskilahti, J. Oksanen, J. Tulkki, and S. Volz, Phys. Rev. B **90**, 134312 (2014).
[59] N. Q. Le, C. A. Polanco, R. Rastgarkafshgarkolaei, J. Zhang, A. W. Ghosh, and P. M. Norris, Phys. Rev. B **95**, 245417 (2017).
[60] E. S. Landry and A. J. H. McGaughey, Phys. Rev. B **80**, 165304 (2009).
[61] X. Gonze and C. Lee, Phys. Rev. B **55**, 10355 (1997).
[62] K. Esfarjani and H. T. Stokes, Phys. Rev. B **77**, 144112 (2008).
[63] D. C. Gazis and R. F. Wallis, Phys. Rev. **151**, 578 (1966).
[64] M. Born and K. Huang, *Dynamical Theory of Crystal Lattices* (Clarendon Press, Oxford, 1998).
[65] G. Kresse and D. Joubert, Phys. Rev. B **59**, 1758 (1999).
[66] J. P. Perdew and A. Zunger, Phys. Rev. B **23**, 5048 (1981).
[67] H. J. Monkhorst and J. D. Pack, Phys. Rev. B **13**, 5188 (1976).
[68] See Supplemental Material at … for the Quantum Espresso scf input files of the interfaces.
[69] H. Schulz and K. H. Thiemann, Solid State Commun. **23**, 815 (1977).
[70] T. Ruf, J. Serrano, M. Cardona, P. Pavone, M. Pabst, M. Krisch, M. D'Astuto, T. Suski, I. Grzegory, and M. Leszczynski, Phys. Rev. Lett. **86**, 906 (2001).
[71] M. Schwoerer-Böhning, A. T. Macrander, M. Pabst, and P. Pavone, Phys. Status Solidi **215**, 177 (1999).
[72] J. M. Zhang, T. Ruf, M. Cardona, O. Ambacher, M. Stutzmann, J.-M. Wagner, and F. Bechstedt, Phys. Rev. B **56**, 14399 (1997).
[73] A. Togo, Https://Atztogo.Github.Io/Spglib/ (n.d.).
[74] C. A. Polanco and L. Lindsay, Phys. Rev. B **97**, 014303 (2018).
[75] C. A. Polanco and L. Lindsay, Phys. Rev. B **98**, 014306 (2018).
[76] M. P. Lopez Sancho, J. M. Lopez Sancho, and J. Rubio, J. Phys. F Met. Phys. **14**, 1205 (1984).
[77] M. P. Lopez Sancho, J. M. Lopez Sancho, J. M. L. Sancho, and J. Rubio, J. Phys. F Met. Phys. **15**, 851 (1985).
[78] G. A. Slack, R. A. Tanzilli, R. O. Pohl, and J. W. Vandersande, J. Phys. Chem. Solids **48**, 641 (1987).
[79] G. A. Slack, L. J. Schowalter, D. Morelli, and J. A. Freitas, J. Cryst. Growth **246**, 287 (2002).